

Article

Effect of High Temperatures on Mechanical and Shielding Properties of Lead–Zinc Tailings Concrete for Radiation Protection

Minghui Wang ^{1,2,3}, Zhenfu Chen ^{1,2,3,*}, Qiuwang Tao ^{1,2,3}, Yan'e Yang ⁴, Liping Xie ⁵, Dan Wu ^{1,2,3}, Dan Jin ^{1,3} and Lincheng Luo ^{1,2,3}

- ¹ School of Civil Engineering, University of South China, Hengyang 421001, China; 20212009110531@stu.usc.edu.cn (M.W.); taoqiuwang@usc.edu.cn (Q.T.); 2017000067@usc.edu.cn (D.W.); jindan@usc.edu.cn (D.J.); 20192009210355@stu.usc.edu.cn (L.L.)
- ² China Nuclear Industry Key Laboratory of High-Performance Concrete, University of South China, Hengyang 421001, China
- ³ Hunan Provincial Key Laboratory of High-Performance Special Concrete, University of South China, Hengyang 421001, China
- ⁴ School of Civil Engineering, Lanzhou University of Technology, Lanzhou 730050, China; 212085900004@lut.edu.cn
- ⁵ China Nuclear Industry 22ND Construction Co., Ltd., Yichang 443101, China; xlp8129@163.com
- * Correspondence: chenzhenfu@usc.edu.cn

Abstract: Due to the high prices, the popularity of radiation shielding concrete (RSC) has been greatly limited. To solve this, this research reused the lead–zinc tailings (LZT) as a fine aggregate replacement ranging from 0% to 60% for the RSC. The results revealed that the RSC containing 30% LZT presented better workability and achieved 95.84% of the compressive strength and 98.49% of the linear attenuation coefficient of the RSC, and reached the highest splitting tensile strength values, which increased by 4.43%. Meanwhile, after the heat treatments, there were favorable correlations between the relative velocity and relative strength, as well as between the damage index and the relative linear attenuation coefficient, which could accurately reflect the degradation of not only the mechanical but also the shielding properties. Considering the temperature and shielding thickness, the reuse of LZT can bring considerable economic and environmental benefits.

Keywords: high temperature; lead–zinc tailings; radiation shielding concrete; mechanical strength; gamma ray shielding; ultrasonic pulse velocity



Citation: Wang, M.; Chen, Z.; Tao, Q.; Yang, Y.; Xie, L.; Wu, D.; Jin, D.; Luo, L. Effect of High Temperatures on Mechanical and Shielding Properties of Lead–Zinc Tailings Concrete for Radiation Protection. *Buildings* **2024**, *14*, 1104. <https://doi.org/10.3390/buildings14041104>

Academic Editor: Dan Bompa

Received: 15 February 2024

Revised: 22 March 2024

Accepted: 11 April 2024

Published: 15 April 2024



Copyright: © 2024 by the authors. Licensee MDPI, Basel, Switzerland. This article is an open access article distributed under the terms and conditions of the Creative Commons Attribution (CC BY) license (<https://creativecommons.org/licenses/by/4.0/>).

1. Introduction

With the deterioration of the natural environment, the negative impact of traditional energy on the environment urgently needs to be addressed. As an emerging form of green power, nuclear energy can almost replace the traditional fossil fuels to mitigate the significant contributions of energy production to ecological degradation. However, there exists a potential risk of nuclear radiation leakage during the utilization of nuclear energy [1]. At present, the majority of materials employed for radiation shielding are heavy concrete, also recognized as radiation shielding concrete (RSC), which typically comprises high-density natural coarse aggregates possessing a specific gravity of 3.0 or greater [2–4]. However, due to the high prices of hematite, barite and magnetite (the main components of high-density natural coarse aggregates), the popularity of RSC has been greatly limited. Therefore, it is crucial to explore a more suitable and cost-effective alternative.

The main difference between RSC and ordinary concrete is the type of aggregates used. Therefore, the paramount objective is to investigate novel materials that demonstrate superior performance across all other parameters while concurrently being more economical. Categorically, these potential substitute compositions can be differentiated based on their

origin into industrial by-products, virgin materials, commercial wastes, domestic refuse and mine tailings [5–9]. Moreover, the large quantities of wastes generated by the iron steel industry, slags produced from iron smelting, slags from blast furnace slag, slags from the smelting of lead–zinc ore and copper slags from copper extraction could be applied as aggregates or cement due to their shared property of retaining heavy elements [10–15]. Furthermore, mine tailings, which are produced in vast amounts annually worldwide, hold immense potential for application in radiation shielding concrete (RSC).

Mineral extraction, an industry deeply entrenched within the global economic framework, is concurrently recognized for its substantial environmental implications [16]. Furthermore, the large volume of tailings stored in tailings dams is also one of the major potential hazards [17,18]. For decades, the catastrophic failure of tailings dams has precipitated severe environmental calamities globally [19–21]. This reality underscores the imperative to regard tailings, a form of solid waste, with the utmost seriousness. Nowadays, research on the use of tailings for building materials is well established [22–25]. Tailings are mainly used in building materials such as clinker production, supplementary cementitious materials (SCMs) and concrete aggregates, etc. Studies have shown that the designed clinker by tailings can control the leaching of heavy metals after hydration [26]. Additionally, the principal issue with employing tailings as cement clinker is that tailings are not normally cemented and are usually accompanied by the reduced strength of the cement and concrete mortars [27]. To address this issue, mechanical activation is considered to be a viable and highly effective treatment method, which can be useful to increase the cementitious activity index and enhance the compressive strength of concrete [28,29]. However, the utilization of tailings in radiation shielding concrete (RSC) requires further systematic research to expand the range of applications for tailings sand. It has been observed that lead mine tailings have a positive influence on the compressive strength when used as a substitute for RSC aggregates [30], and barite–fluorspar mine waste (BFMW) is also beneficial to the compressive strength of radiation shielding cement mortar [31]. The reason why there is no significant linear increase or decrease in the radiation absorption coefficients of the mixed aggregates can be attributed to the variability of the lead content in the tailings [32]. Similarly, the incorporation of lead–zinc tailings sand (LZT) into plain concrete follows a similar trend [33,34].

Over the course of its operational lifespan, RSC may be exposed to high temperatures, so the determination of heat distribution and heat effect or thermal stress is a significant aspect of the shielding design [35]. Heavy concretes with aggregates of ilmenite, magnetite and hematite have good phase stability when exposed to high temperatures [36–38]. The reason why the mechanical and shielding properties of heavy concrete deteriorate is mainly due to the loss of crystalline water, the development of internal cracks [39] and severe bursting phenomena [36,37,40]. For ultra-high-performance concrete (UHPC), the bursting phenomenon is more serious [41]. Meanwhile, the crystalline water directly affects the neutron shielding ability of RSC, owing to its hydrogen content [42–44]. But there is currently a lack of research on the effect of high temperatures on RSC mixed with tailings sand.

As the accumulation of old tailings sand continues unabated within tailings dams, and with the ongoing production of new tailings sand, there exists a pressing need to further broaden the application scope of tailings sand. To solve this problem, this literature study investigated the reuse of lead–zinc tailings sand (LZT) as a fine aggregate replacement ranging from 0% to 60% for magnetite radiation shielding concrete, whose workability, mechanical performance (including compressive strength and splitting tensile strength) and γ -ray shielding performance have been studied. Afterwards, in consideration of the possibility that radiation shielding concrete (RSC) may encounter high-temperature exposure during its operational lifetime, this paper also opts for the concrete mix with superior overall performance to conduct a high-temperature trial aimed at examining the residual capabilities. Meanwhile, throughout this experiment, ultrasonic nondestructive testing was employed to indirectly assess and evaluate the degradation of the mechanical

performance and γ -ray shielding performance of the lead–zinc tailings sand radiation shielding concrete (LZTRSC) after exposure to elevated temperatures.

2. Raw Materials and Test Methods

2.1. Raw Materials

- (1) **Cement:** The experiments employed ordinary Portland P.O 42.5 cement, which was procured from Hunan Province in China. The chemical constituents of the utilized cement are delineated in Table 1. The cement possesses a density of 3100 kg/m³ and a fineness value of 370 m²/kg. For the relevant regulations, we referred to Common Portland Cement (GB 175-2007) [45].

Table 1. Chemical composition of the cement and the used aggregates (wt.%).

Composition	Na ₂ O	MgO	Al ₂ O ₃	SiO ₂	SO ₃	CaO	MnO	Fe ₃ O ₄	Fe ₂ O ₃	ZnO	PbO	LOI
Cement	0.18	2.78	5.24	17.88	0.95	68.38	-	-	2.33	-	-	2.25
LZT	0.19	1.47	6.83	76.91	5.45	2.88	0.17	-	4.02	0.26	0.19	1.64
Magnetite	0.46	2.43	3.24	7.90	0.72	2.68	0.23	80.52	-	0.05	0.04	1.73

The above data in Table 1 come from www.eceshi.com.

- (2) **Aggregates:** The test methods employed in this study adhere to the standards outlined in Sand for Construction (GB/T 14684-2022) [46] and Pebble and Crushed Stone for Construction (GB/T 14685-2022) [47]. The lead–zinc tailings sand (LZT) and magnetite aggregates were sourced from a tailings dam located in Shuikou Mountain, Hunan Province, China, and Henan Province, China, respectively. To prepare the LZT, which was initially stored in a wet state, it was dried in an oven at 105 °C for 24 h and subsequently sieved. The magnetite coarse and sand aggregates underwent washing and were then naturally dried in an open outdoor area for one week. These aggregates were then sieved using standard square-hole sieves, with needle-like and flaky stones being removed. Magnetite coarse aggregates with a maximum particle size of 20 mm were prepared and proportioned according to standardized mass ratios. Magnetite fine aggregates were obtained by sieving magnetite sand with a particle size range of 0–5 mm. The principal chemical composition and fundamental properties of the aggregates are detailed in Tables 1 and 2, respectively. The grading curves for both coarse and fine aggregates are depicted in Figure 1.

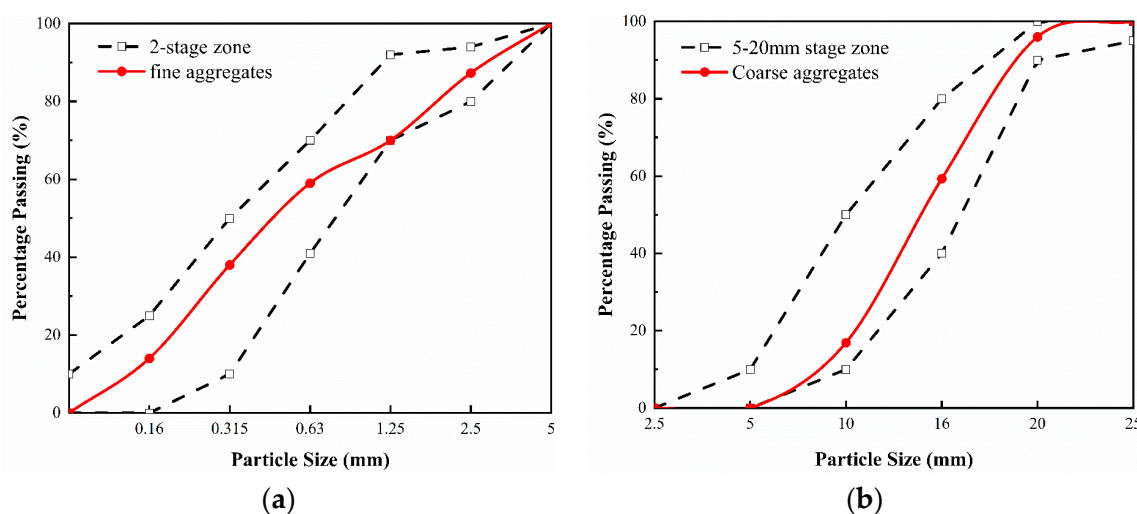


Figure 1. Particle size distribution of the used aggregates: (a) fine aggregates; (b) coarse aggregates.

Table 2. Basic properties of the aggregates.

Aggregate Type	Particle Size (mm)	Apparent Density (kg/m ³)	Crush Index (%)	Water Absorption (%)	Water Content (%)
LZT	0–0.6	2620.00	-	6.10	10.80
Magnetite	0–5	4620.00	-	0.70	0.20
	5–20	4440.00	7.10	0.20	0.10

The above data in Table 2 were obtained from the test followed in GB/T 14684-2022 and GB/T 14685-2022.

(3) Water: Tap water was supplied within the laboratory premises.

2.2. Mix Proportion and Specimen Arrangement

The initial mix proportion was derived from the mix ratio standard specified in GB/T 34008-2017 [48]. After a series of preliminary trials, an optimal mixing ratio for the radiation shielding concrete (RSC) was achieved, as detailed in Table 3.

Table 3. Mix proportion of the concrete.

LZT Ratio (%)	Water–Binder Ratio	Mix Proportion (kg/m ³)				
		Cement	LZT	Magnetite Sand	Magnetite Coarse	Water
0			0	1077.8		
10			100.1	901.3		
20			187	748.1		
30	0.54	398	263.1	613.9	1835.2	215
40			330.3	495.4		
50			390	390		
60			443.6	295.7		

A total of 156 RSC specimens, each measuring 100 × 100 × 100 mm, were prepared for testing. Of these, 84 specimens were designated for room-temperature tests, while the remaining 72 were allocated for high-temperature tests. The RSC samples were removed from their molds 24 h post-casting and subsequently cured in a standardized environment for a period of 28 days. Upon completion of the curing process, the test blocks were promptly extracted for immediate testing.

2.3. Test Methods

2.3.1. Work Performance Test

The working performance of the concrete was assessed by examining the consistency of the concrete slurry, which included measurements of the slump, the extent of water separation and the degrees of delamination and segregation. Table 4 presents the results of the slump test.

Table 4. Results of the concrete mix consistence slump test.

LZT Ratio (%)	Cohesion	Bleeding	Slump Values (mm)	Slump Class
0	Poor		2	
10	Slightly poor		15	
20	Plain	None of them	17	
30	Good	have obvious	20	S1
40	Good	water bleeding	16	
50	Good	phenomena	8	
60	Good		7	

2.3.2. High-Temperature Heating Test

The experiment was performed using an SX2-36-13-1300 °C chamber muffle furnace (Fenghua Industrial Furnace Factory, Xinghua, China). A heating rate of 3.5 °C/min was employed to attain the desired temperatures of 200, 300, 450, 600 and 800 °C, respectively. The test commenced from a room temperature of 25 °C (the external surface temperature of the specimen reached the target temperature) and subsequently maintained the target temperature for a duration of 2 h. Figure 2 illustrates the high-temperature test's heating process diagram.

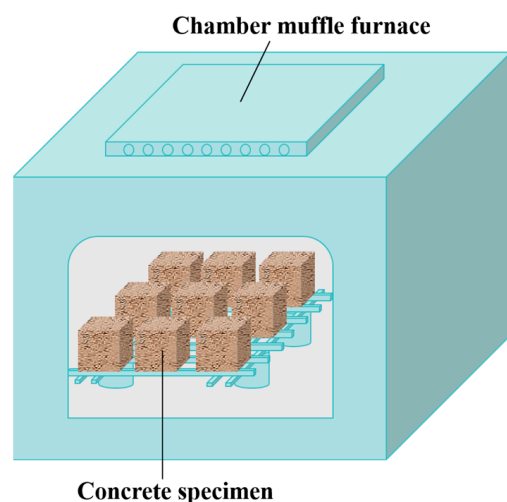


Figure 2. Diagram of the muffle furnace heating process.

2.3.3. Mechanical Test

The WAW-EY1000C (Jinan Shijin Group Co., Ltd., Jinan, China) microcomputer-controlled electro-hydraulic servo universal testing machine was utilized for the evaluation of the mechanical strength in the concrete during the mechanical testing. The cube compressive strength test was executed using stress-controlled loading at a rate of 0.5 MPa/s, while the splitting tensile strength test was conducted with stress-controlled loading at a rate of 0.05 MPa/s, adhering to the Standard for Test Method of Concrete Physical and Mechanical Properties (GB/T 50081-2019) [49].

2.3.4. Ultrasonic Nondestructive Testing

The experiment was performed using a non-metallic ultrasonic detector (ZBL-U5200, Beijing Zhibolian Technology Co., Ltd., Beijing, China) on a 100 mm concrete cube specimen. The detector had a sampling period of 0.4 μ s, an acoustic time accuracy of 0.025 μ s, a reception sensitivity of no more than 10 μ V and a gain accuracy of 0.5 dB. The transducer frequency used was 45 kHz. The pair test method was employed to derive the wave velocity parameter, as depicted in Figure 3. To enhance data precision, an ultrasonic coupling agent was uniformly applied to the contact areas between the ultrasonic detector probe and the specimen. Additionally, to ensure the accuracy of the specimen's actual damage state, nine measurement zones were evenly selected on the specimen (as shown in Figure 3). Each measurement zone was measured three times to calculate the mean value. The testing methodology adhered to the Technical Specification for Inspection of Concrete Defects by Ultrasonic Method (CECS21:2000) [50].

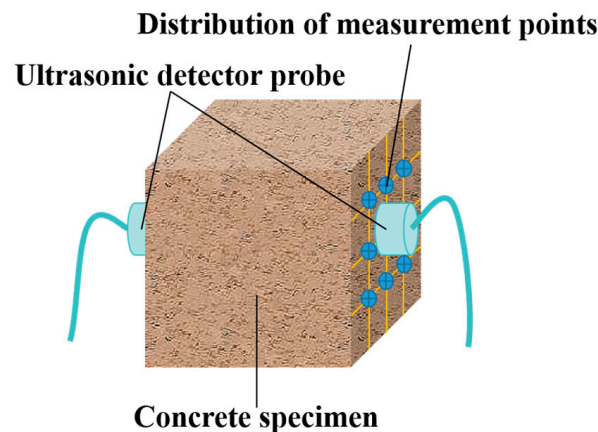


Figure 3. Diagram of the ultrasonic pair measurement method.

2.3.5. γ -ray Shielding Test

The BH-1326 nuclear physics testing platform was utilized to perform the γ -ray shielding test, utilizing a γ -ray source that emitted 0.662 MeV photon energy from the ^{137}Cs radioisotope. The objective of the test was to assess the attenuation of γ -rays in the RSC. Concrete samples measuring 100×100 mm with varying thicknesses of 25, 50, 75, 100 and 125 mm were employed as experimental specimens. In addition, the test block was partitioned into 9 measurement zones, with each zone being subjected to γ radiation three times and with each exposure lasting 60 s. The mean value of the measurements was subsequently computed for each area. Figure 4 illustrates the schematic of the γ -ray shielding test apparatus. The linear attenuation coefficient (μ) of the RSC was derived from the Lambert–Beer law, as depicted in Equation (1). The mass attenuation coefficient (μ_m) was obtained from Equation (2), while the mean free path (Mfp) was calculated using Equation (3). The thicknesses of the half-value layer (HVL) and tenth-value layer (TVL) typically contribute to the assessment of the material's γ -ray shielding efficacy [51], as defined by the necessary thickness of the RSC when the γ -ray intensity diminishes to half and one-tenth of the initial emission value, respectively [52], which can be determined using Equations (4) and (5). Finally, the transmission rate can be derived from Equation (6).

$$I = I_0 e^{-\mu x} \quad (1)$$

$$\mu_m = \frac{\mu}{\rho} \quad (2)$$

$$\text{Mfp} = \frac{1}{\mu} \quad (3)$$

$$\text{HVL} = \frac{\ln 2}{\mu} \quad (4)$$

$$\text{TVL} = \frac{\ln 10}{\mu} \quad (5)$$

$$\text{Transmission rate} = \frac{I}{I_0} \quad (6)$$

where I represents the γ -ray counting rate after transmission through a concrete sample of thickness x ; I_0 represents the initial counting rate without the sample in place; x is the thickness of the RSC sample (cm); μ is the linear attenuation coefficient of the RSC sample (cm^{-1}); μ_m is the mass attenuation coefficient of the RSC sample (cm^2/g); ρ is the density of the RSC sample (g/cm^3).

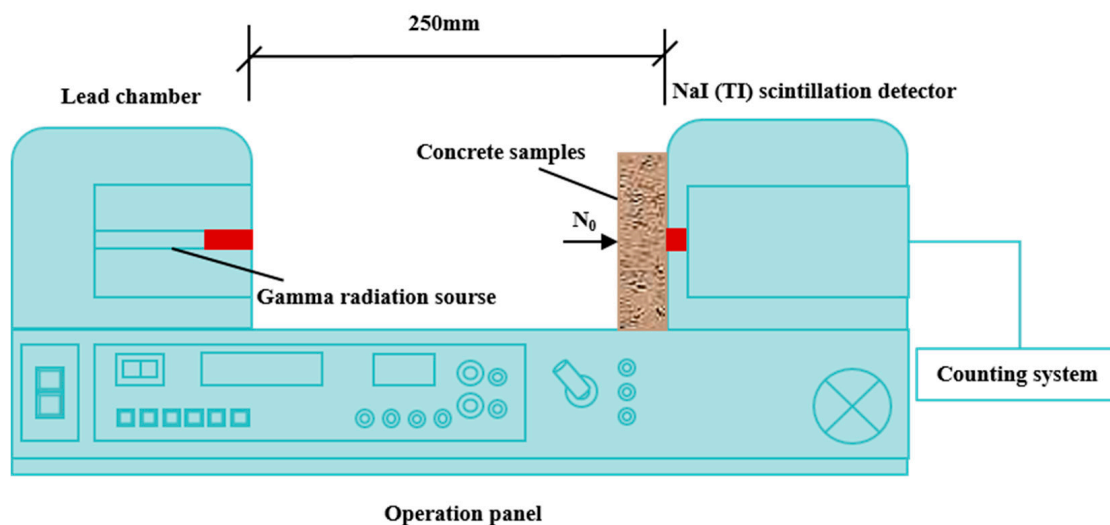


Figure 4. Diagram of the γ -ray shielding test equipment.

3. Results and Discussion

3.1. Properties of Radiation Shielding Concrete with Different LZT Ratios at Room Temperature

3.1.1. Workability

The slump values of the concrete slurries with varying LZT ratios are presented in Table 4. As indicated in Table 4, the slump value of the concrete slurry initially increased and then decreased as the substitution ratio increased. The optimal substitution ratio is identified as 30%. This phenomenon can be explained by the fact that a small amount of LZT fine particles can fill the voids, leading to an increase in the amount of free water in the system and, consequently, improving the fluidity of the mixture. However, due to the relatively large specific surface area of the LZT, more free water is required in the slurry as the LZT dosage increases. This counteracts the water-reducing effect caused by the filling effect, resulting in reduced fluidity [38,53].

3.1.2. Compressive Strength

The 28d compressive strength (f_c) of the concrete with various LZT replacement ratios is depicted in Figure 5. It is evident that the compressive strength of the concrete slightly decreases as the LZT content increases, particularly when the substitution ratio is below 30%. Concrete with a 30% LZT admixture exhibits a compressive strength of 95.84% relative to the control group (0% LZT). However, the strength begins to diminish rapidly beyond this point, dropping to 75.27% of the control group's strength at a 60% admixture ratio. This deterioration in strength could be attributed to the lower density and strength of the LZT compared to the magnetite sand. Moreover, the LZT contains a high level of sulfides, which react with cement to form calcium sulfate. This reaction results in a reduction in C-S-H and other cement hydration products, which are essential for cohesion and concrete strength [54]. Additionally, it is important to note that, although LZT is categorized as a type of fine aggregate, its particles are smaller and have a larger specific surface area compared to magnetite sand due to its unique origin. As the LZT dosage increases, the particles act as fillers, potentially enhancing the slurry content in the mix and improving the workability of the magnetite concrete. The optimal workability is attained at a 30% LZT dosage. However, as the substitution ratio continues to rise, an increased amount of LZT fine particles necessitates additional water consumption, leading to a decline in the compressive strength. When the substitution ratio surpasses 40%, the concrete gradation worsens, culminating in a significant drop in the compressive strength.

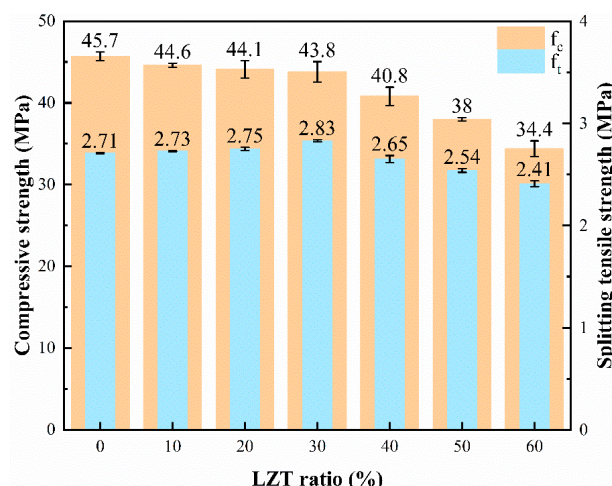


Figure 5. Strength of the concrete with different LZT ratios.

3.1.3. Splitting Tensile Strength

Figure 5 demonstrates the splitting tensile strength (f_t) at room temperature for varying percentages of the LZT replacement. Initially, the splitting strength increases and then decreases as the LZT replacement ratio rises. The peak strength is observed at a 30% replacement level, where there is a 4.40% increase in comparison to the control sample. As the LZT ratio continues to escalate, the strength gradually diminishes. At a 60% replacement ratio, the strength falls to 88.93% of the control value. The initial enhancement in splitting tensile strength can be attributed to the improved workability achieved with an optimal LZT replacement ratio. However, the subsequent reduction in strength may result from the detrimental effects on the gradation, which outweigh the positive impacts of the improved fluidity in the mixture.

3.1.4. Ultrasonic Pulse Velocity

When defects such as holes or cracks are present in the propagation path of an ultrasonic pulse, its pattern alters, leading to a decrease in wave velocity [55]. Consequently, ultrasonic flaw detection techniques can be employed to investigate and evaluate the degree of internal densification, and to infer the porosity and compressive strength [56]. Additionally, the ultrasonic wave velocity can be used to assess the damage and degradation of the concrete following heat treatment. The concrete's durability diminishes due to cracking, spalling, bursting and the gradual degradation of the hardened cement paste [57], which in turn affects the ultrasonic pulse rate [58,59]. Figure 6 depicts the variation in the ultrasonic wave velocity for the concrete with different LZT replacement ratios. The wave velocity tends to increase initially and then decrease as the LZT substitution ratio rises. It remains relatively stable below a 30% admixture, but beyond this point, the rate of decrease accelerates. This phenomenon can be attributed to the finer LZT particles, which can reduce the inner pores of the concrete [6]. However, once the substitution ratio surpasses 30%, the workability of the concrete slurry deteriorates, followed by a worsening of the gradation conditions, resulting in an increase in the number of voids within the concrete and a concomitant decline in the ultrasonic wave velocity [55].

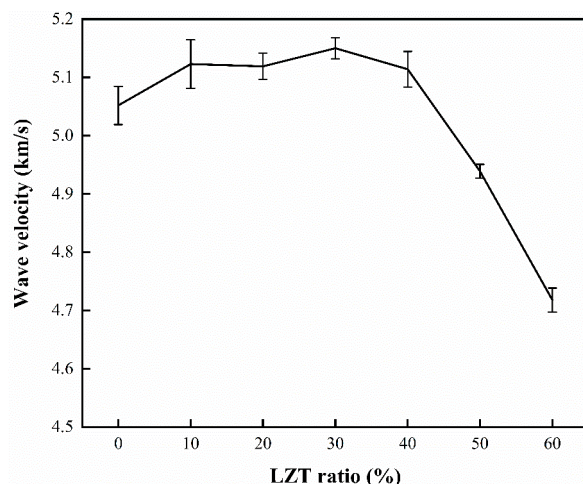


Figure 6. Wave velocity of the concrete with different LZT ratios.

3.1.5. γ -ray Shielding Performance Results and Analysis

The results presented herein derive from concrete samples with a uniform thickness of 10 cm. In Table 5, μ is the linear attenuation coefficient, μ_m is the mass attenuation coefficient, Mfp is the mean free path, HVL is the thickness of half-value layer, TVL is the thickness of tenth-value layer and the relative coefficient is the percentage of the linear attenuation coefficient for different doping levels versus the control group (0% LZT). The absence of a value after the \pm sign indicates that the standard error is less than one-thousandth.

Table 5. Test results of the γ -ray shielding test with different LZT ratios at room temperature.

LZT Ratio (%)	μ (cm^{-1})	μ_m (cm^2/g)	Mfp (cm)	HVL (cm)	TVL (cm)	Relative Coefficient (%)
0	0.265	0.075	3.767 \pm 0.002	2.611 \pm 0.001	8.673 \pm 0.004	100
10	0.264	0.075	3.784 \pm 0.002	2.623 \pm 0.001	8.714 \pm 0.004	99.594
20	0.264	0.076	3.793 \pm 0.005	2.629 \pm 0.004	8.734 \pm 0.013	99.465
30	0.261 \pm 0.001	0.077	3.825 \pm 0.008	2.651 \pm 0.005	8.808 \pm 0.018	98.440
40	0.260	0.078	3.842 \pm 0.006	2.663 \pm 0.004	8.848 \pm 0.015	97.982
50	0.259	0.078	3.865 \pm 0.001	2.679 \pm 0.001	8.899 \pm 0.003	97.514
60	0.256	0.078	3.910 \pm 0.003	2.710 \pm 0.002	9.003 \pm 0.007	96.405

The relationship between the thickness of the concrete sample and $\ln(I/I_0)$ is depicted in Figure 7. By analyzing the slope of the regression line between $\ln(I/I_0)$ and the thickness of the concrete sample, the μ of the concrete specimen was acquired. Considering the commonly used test block sizes specified in the standard (GB/T 50081-2019), this paper mainly shows the results of the test block size of 10 cm with different LZT ratios (Table 5). The consequences indicate that the μ of the RSC doped with LZT declines with the enhancement of the LZT ratio. However, the decrease is not significant, and the μ of the 60% dosage can reach 96.60% of the control group (0% group). This can be attributed to the improvement in the workability of the RSC and the finer fineness of the LZT fine particles. Despite its lower density, which reduces the overall density of the RSC [60], the LZT produces a less porous concrete specimen. This trend can also be explained according to the ultrasonic wave velocity shown in Figure 6. Additionally, the LZT admixture introduces a small amount of heavy metals, such as Pb and Zn, which may compensate to some extent for the increase in the LZT admixture [32]. These factors contribute to the γ -ray shielding property of the LZT radiation shielding concrete. Figure 8 illustrates the relationship between the γ -ray transmission rate and the thickness of the LZT radiation shielding concrete. The results demonstrate that, at the same γ -ray transmittance rate, the minimum thickness

required for the effective shielding of the RSC doped with LZT increases with the LZT dosage. Therefore, in practical engineering applications, selecting an appropriate thickness for the shielding layer, and with 30% of the fine aggregate replacement of the radiation shielding concrete, can yield significant economic and environmental benefits. The γ -ray shielding performance is comparable to that of pure magnetite RSC.

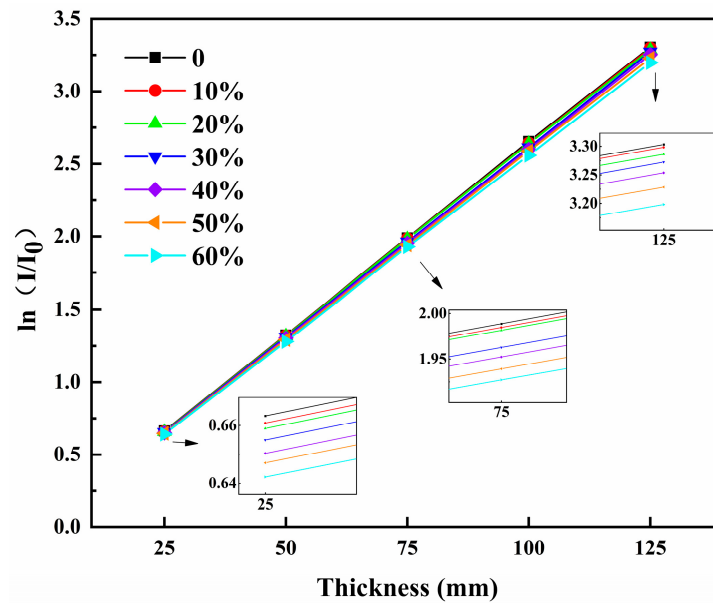


Figure 7. Relationship between concrete thickness and $\ln(I/I_0)$ at room temperature.

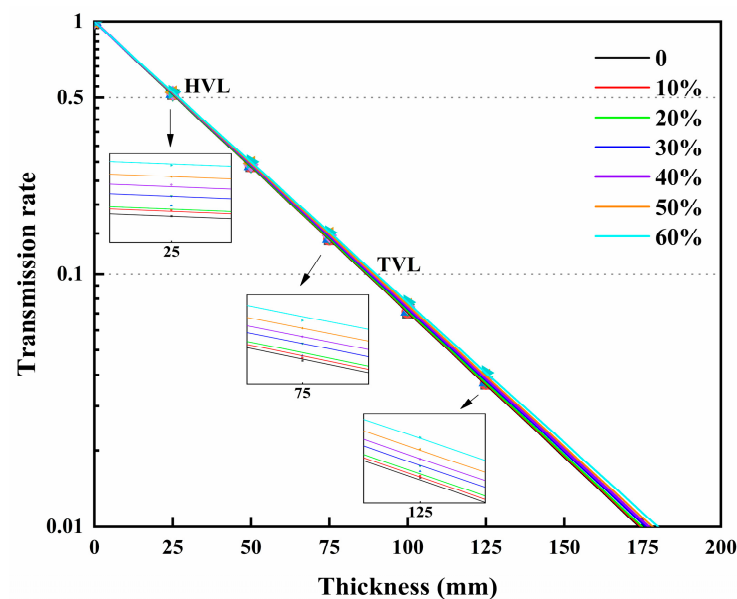


Figure 8. Relationship between concrete thickness and the γ -ray transmission rate at room temperature.

Based on the above results, it was found that replacing magnetite sand with 30% of LZT as fine aggregates for RSC does not significantly reduce the compressive strength and γ -ray shielding performance of the RSC. It can also improve the workability and splitting tensile strength. Considering the cost, the magnetite used in the experiment is raw ore, while the LZT belongs to solid wastes, which has a very low cost. The accumulation of LZT may also cause serious safety accidents and environmental pollution. If used widely, it will bring considerable economic and environmental benefits.

In practical applications, RSC may be subjected to both radiation and elevated temperatures simultaneously over the course of its operational lifespan. For instance, in certain

nuclear facilities, the inner surface of concrete is often directly exposed to temperatures as high as 150 °C for extended periods, while some nuclear reactors may reach temperatures as high as 400 °C [12,36,61]. Taking into account the effect of elevated temperatures, this study integrated the workability, mechanical performance and γ -ray shielding performance of RSC and conducted the high-temperature test on the lead–zinc tailings sand radiation shielding concrete with a 30% admixture. The experimental results are as follows.

3.2. Properties of Lead–Zinc Tailings Radiation Shielding Concrete (LZTRSC) Exposed to Elevated Temperatures

3.2.1. Failure Characteristics

The apparent observations of the LZTRSC samples after the heat treatment are presented in Figure 9. The results indicate that the LZTRSC specimens display a limited number of short-segment microcracks on their exterior surface when the temperature rises from 200 °C to 450 °C. A substantial increase in the number of microcracks is noted at 450 °C, and these continue to propagate. At 600 °C, noticeable short-segment cracks begin to form and extend. Wider cracks are observed at 800 °C, accompanied by bursts and spalling in specific areas. The heat treatment results clearly demonstrate that the appearance of LZTRSC progressively deteriorates with increasing temperature.



Figure 9. Appearance of the LZTRSC specimen exposed to elevated temperatures.

3.2.2. Mass Loss

The variations in the mass (M) and the density (ρ) of the LZTRSC after exposure to elevated temperatures are presented in Table 6, which indicates that the mass of the LZTRSC declines as the temperature grows due to the transformations occurring within the material. After exposure to a temperature of 200 °C, the concrete mass loss is 3.88%, while the mass stabilizes between 200 °C and 300 °C. This stabilization is primarily due to the evaporation of free water and the water of crystallization in the hydration products of the concrete. Furthermore, the mass loss at 450 °C, 600 °C and 800 °C is 5.08%, 5.69% and 6.86%, respectively. With the rise in temperature from 450 °C to 600 °C, the cement hydration products undergo decomposition, leading to a significant decrease in mass [62]. When the temperature is raised from 600 °C to 800 °C, the decomposition of CaCO_3 and the polycrystalline transformation of the aggregate occur [63–65]. These processes result in the bursting and spalling of the concrete, consequently leading to a substantial mass loss.

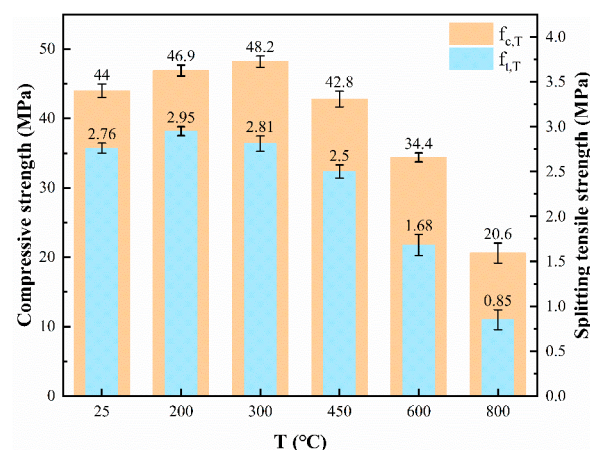
Table 6. Mass (M), density (ρ) and wave velocity (V) of the LZTRSC at different temperatures.

T (°C)	M (g)	ρ (kg/m ³)	V (km/s)
25	3366.25 ± 3.41	3337.13 ± 7.53	5.150 ± 0.02
200	3235.38 ± 3.31	3232.63 ± 9.54	4.361 ± 0.04
300	3231.67 ± 3.62	3221.60 ± 6.27	4.283 ± 0.03
450	3195.40 ± 5.95	3223.46 ± 9.90	3.475 ± 0.04
600	3174.84 ± 5.73	3190.74 ± 24.23	2.343 ± 0.06
800	3135.44 ± 8.31	3138.29 ± 18.98	1.932 ± 0.09

3.2.3. Compressive Strength

There are three mechanical test methods, including transient, steady-state and residual tests, after high-temperature treatment [66]. The test method used in this research is the residual test.

The remaining compressive strength ($f_{c,T}$) of the LZTRSC after exposure to different temperatures is given in Figure 10. The result of the test indicates that the remaining compressive strength of the LZTRSC after exposure to different high temperatures follows a trend of initially increasing and then declining. At 300 °C, the compressive strength increases by 9.55% compared to the control group at room temperature (25 °C). The increase can be due to the rehydration of unhydrated cement particles in the concrete stimulated by the high temperatures from 200 °C to 300 °C [67]. Meanwhile, the removal of absorbed water in the concrete increases the surface force between the cementitious particles, which further enhances the compressive strength [68]. However, as the temperature exceeds 300 °C, cracks begin to form between the different aggregates, as well as between the aggregates and the products of cement hydration, due to the different coefficients of expansion at high temperatures. At 450 °C, the compressive strength decreases by 2.73% compared to the control group. From 450 °C to 600 °C, the decomposition of $\text{Ca}(\text{OH})_2$ as well as the increase in and extension of cracks lead to a residual compressive strength of only 78.18% of the room-temperature strength when the temperature is up to 600 °C. When the temperature exceeds 600 °C, the decomposition of CaCO_3 and the polycrystalline transformation of aggregates occurs [63–65]. The results indicate that the wider cracks, localized bursting and spalling have a role in the continuous decline in the compressive strength. At 800 °C, the compressive strength drops to only 46.82% of the room temperature.

**Figure 10.** Remaining strength of the LZTRSC after exposure to high temperatures.

3.2.4. Splitting Tensile Strength

As shown in Figure 10, it is known that the remaining splitting strength ($f_{t,T}$) of the LZTRSC does not decline, but rather slightly increases after exposure to temperatures below 300 °C. At 200 °C, the residual splitting tensile strength reaches its highest point, with a 6.88% increase compared to the control group (at room temperature). The splitting strength

then decreases at 300 °C, but it still remains slightly higher than at room temperature. However, when exposed to 450 °C, the splitting strength decreases by 9.42% compared to the control group. Similarly, at 600 °C, as well as at 800 °C, the splitting strength declines to 60.87% and 30.80% of the room temperature, respectively. The major reasons for the decline in the splitting strength are similar to those for the remaining compressive strength.

Having determined the remaining $f_{t,T}$ of the LZTRSC, a comparison study was made using the results of the concrete specimens from the published literature, as shown in Table 7. From Table 7, it can be seen that, when the temperature is lower than 600 °C, the $f_{t,T}$ of the LZTRSC decreases slowly, while the decline is significantly more severe than the MC when the temperature ranges from 600 °C to 800 °C. This may be due to the fact that the inclusion of LZT results in a denser and more homogeneous microstructure, which enhances the resistance of the RSC to elevated temperatures [69]. But the development of enlarged cracks with a less intact microstructure in the RSC when the temperature ranges from 600 °C to 800 °C leads to the severe decline of $f_{t,T}$ [70].

Table 7. Experimental results.

Reference	Specimen ID	Fine Aggregates	Coarse Aggregates	T (°C)	$f_{t,T}$	Relative $f_{t,T}$ (%)
[37]	Magnetite concrete (MC)	Magnetite	Magnetite	25	2.60 ± 0.08	100.00
				300	2.39 ± 0.07	91.92
				450	2.16 ± 0.08	83.08
				600	1.37 ± 0.06	52.69
				800	1.00 ± 0.05	38.46
Current research	LZTRSC	70% Magnetite and 30% LZT	Magnetite	25	2.76 ± 0.06	100.00
				300	2.81 ± 0.09	101.81
				450	2.50 ± 0.07	90.58
				600	1.68 ± 0.12	60.87
				800	0.85 ± 0.11	30.80

3.3. Ultrasonic Nondestructive Testing Results and Analysis

In order to establish a link between the ultrasonic wave velocity and the mechanical properties of the LZTRSC, this paper investigates the relationship between the relative wave velocity and the relative strength after high-temperature treatment with reference to related studies [37,58]. The wave velocity (V) of the LZTRSC after exposure to elevated temperatures is provided in Table 6. The relative ultrasonic wave velocity, relative compressive strength and relative splitting strength were obtained after normalization, as shown in Figures 11 and 12.

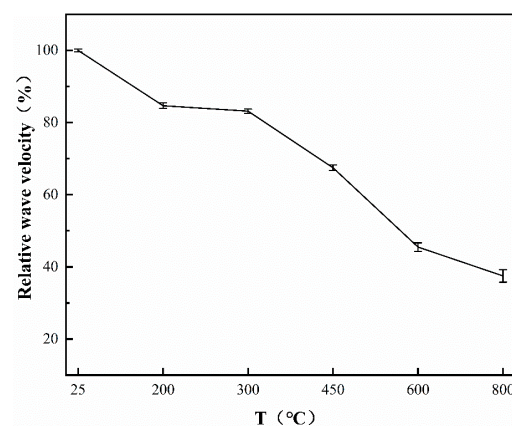


Figure 11. Relative wave velocity of the LZTRSC at different temperatures.

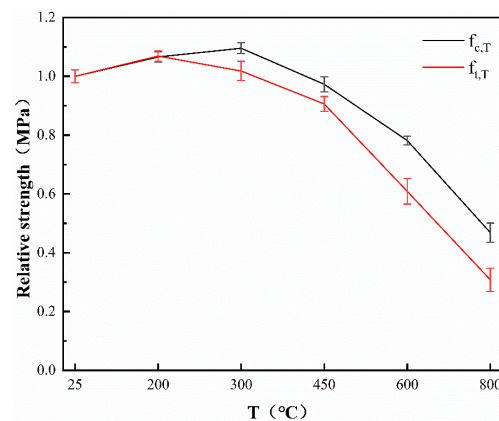


Figure 12. Relative compressive strength ($f_{c,T}$) and relative splitting strength ($f_{t,T}$) of the LZTRSC at different temperatures.

According to Table 6, the ultrasonic wave velocity of the LZTRSC decreases as the temperature increases, while the strength initially slightly enhances and then declines. This is mainly owing to the fact that lower temperatures (below 350 °C) may not significantly affect the mechanical performances but enhance the inhomogeneity of the concrete [60]. As is indicated in Figure 11, the wave velocity declines more significantly at 200 °C, with a decrease of 15.32%. However, there is almost no obvious change in the wave velocity from 200 °C to 300 °C. The wave velocity at 450, 600 and 800 °C decreases to 67.48%, 45.50% and 37.51% of the room temperature, respectively. Notably, the wave velocity decreases the most from 450 °C to 600 °C, with a decrease of 21.98%. This can be attributed to the decomposition of a significant quantity of cement hydration products [62].

3.4. Relationship between Relative Compressive Strength as Well as Relative Splitting Strength and Relative Wave Velocity

The relationships between the relative compressive strength as well as relative splitting strength and relative wave velocity are depicted in Figures 13 and 14, respectively. Regression analysis was performed using an appropriate function, whose fitting consequences are recorded in Figures 13 and 14. The consequence indicates that, as the temperature increases, the mechanical performance gradually deteriorates, accompanied by a decline in the wave velocity. Meanwhile, the relative wave velocity demonstrates a good fit with the two mechanical parameters, with R^2 values greater than 0.95. Therefore, the ultrasonic wave velocity can be effectively applied in evaluating the remaining compressive strength and splitting strength of the LZTRSC after exposure to elevated temperatures.

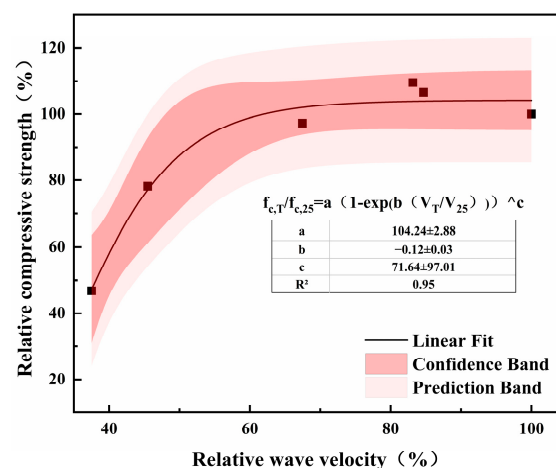


Figure 13. Relationship between the relative velocity and relative compressive strength.

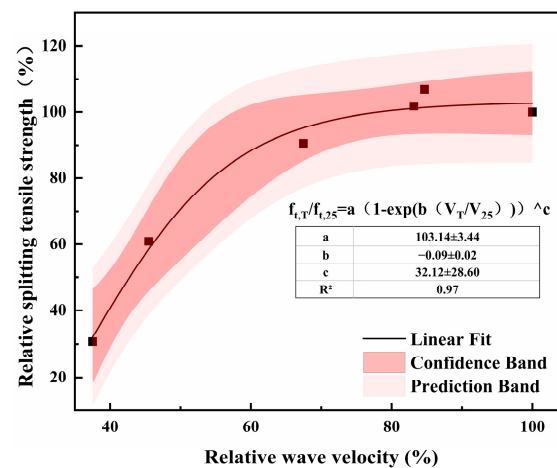


Figure 14. Relationship between the relative velocity and relative splitting strength.

where $f_{c,T}$ and $f_{c,25}$ represent the compressive strength of LZTRSC subjected to different temperatures; $f_{t,T}$ and $f_{t,25}$ represent the splitting strength of LZTRSC subjected to different temperatures; V_T and V_{25} represent the wave velocity of LZTRSC specimens subjected to different temperatures.

3.5. Shielding Performance Results and Analysis

The results presented herein derive from concrete samples with a uniform thickness of 10 cm. In Table 8, μ is the linear attenuation coefficient, μ_m is the mass attenuation coefficient, Mfp is the mean free path, HVL is the thickness of half-value layer, TVL is the thickness of tenth-value layer and the relative coefficient is the percentage of the linear attenuation coefficient at different temperatures compared to the control group (at 25 °C). The absence of a value after the \pm sign indicates that the standard error is less than one-thousandth.

Table 8. Test results of the γ -ray shielding of the LZTRSC exposed to elevated temperatures.

T (°C)	μ (cm^{-1})	μ_m (cm^2/g)	Mfp (cm)	HVL (cm)	TVL (cm)	Relative Coefficient (%)	
						Current Research	[37]
25	0.264 ± 0.001	0.079	3.793 ± 0.009	2.629 ± 0.006	8.734 ± 0.020	100.000	100.000
200	0.259 ± 0.001	0.080	3.867 ± 0.011	2.680 ± 0.008	8.904 ± 0.026	97.996	-
300	0.255	0.079	3.929 ± 0.008	2.724 ± 0.005	9.047 ± 0.018	96.481	96.665
450	0.251 ± 0.001	0.078	3.977 ± 0.012	2.757 ± 0.008	9.158 ± 0.028	95.245	93.360
600	0.246 ± 0.002	0.077	4.070 ± 0.031	2.821 ± 0.021	9.372 ± 0.071	93.194	91.997
800	0.239 ± 0.001	0.076	4.193 ± 0.025	2.906 ± 0.018	9.654 ± 0.058	90.448	89.558

The relationship curve between the thickness of the LZTRSC samples and $\ln(I/I_0)$ after exposure to high temperatures is presented in Figure 15, from which the μ was obtained on the basis of the slope of the curve. Considering the commonly used test block sizes specified in the standard (GB/T 50081-2019), this paper mainly shows the results of the test block size of 10 cm at different temperatures (Table 8). Figure 16 shows the relationship between the thickness and γ -ray transmission rate after exposure to high temperatures. The μ and μ_m of the diverse thicknesses of the concrete are shown in Figures 17 and 18, respectively. Figures 19 and 20 show the changes in the thickness of the HVL and the thickness of the TVL after heat treatment.

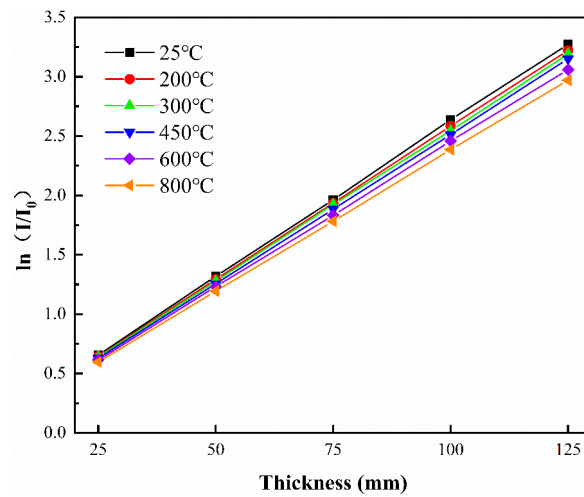


Figure 15. Relationship between the thickness and $\ln(I/I_0)$ after exposure to high temperatures.

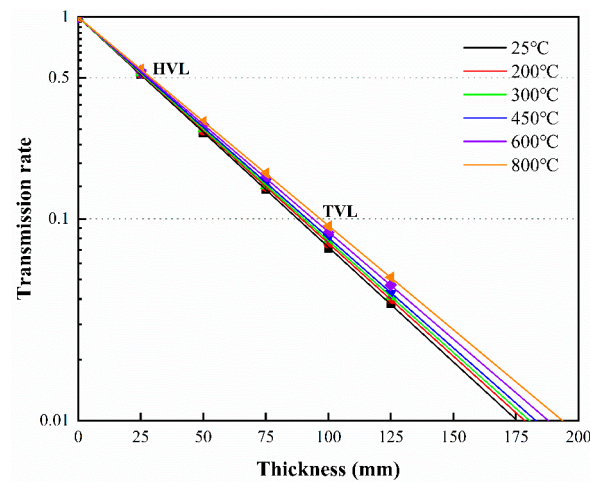


Figure 16. Relationship between the thickness and γ -ray transmission after exposure to high temperatures.

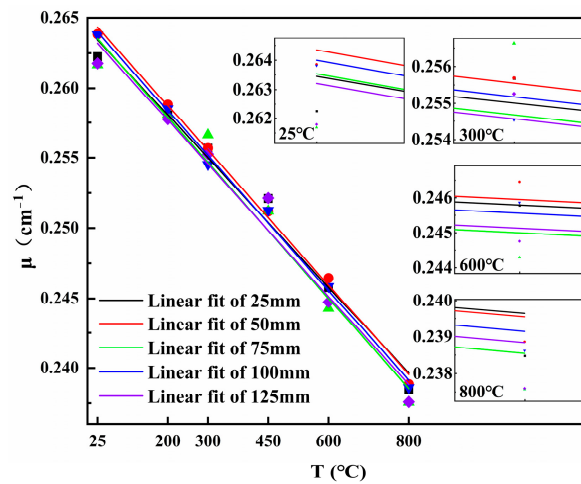


Figure 17. Linear attenuation coefficient of the concrete after exposure to high temperatures.

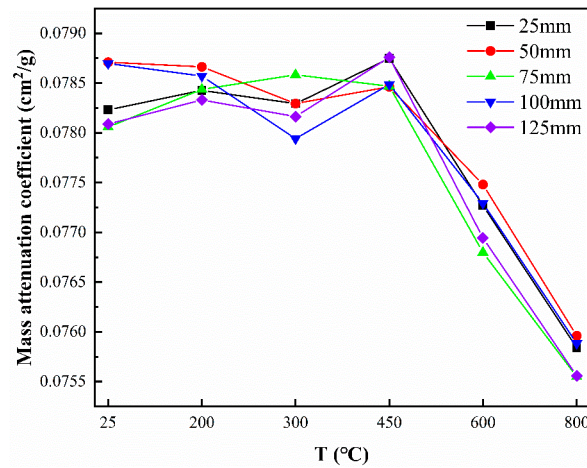


Figure 18. Mass attenuation coefficient after exposure to high temperatures.

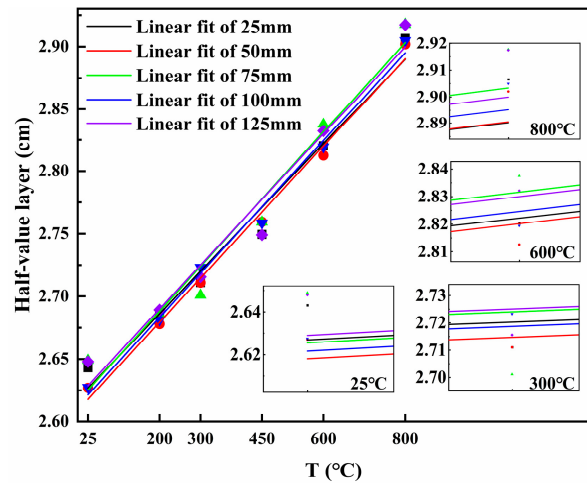


Figure 19. Half-value layer thickness after exposure to high temperatures.

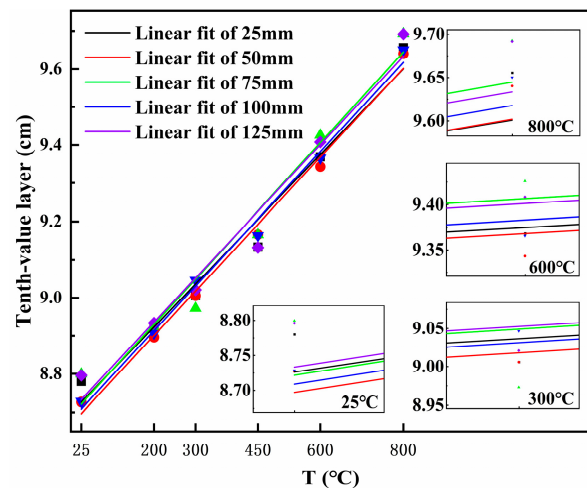


Figure 20. Tenth-value layer thickness after exposure to high temperatures.

The μ of the LZTRSC shows a linearly decreasing trend with the increase in the temperature. The μ_m presents a stable tendency below 450 °C, then decreases linearly. On the contrary, the thickness of the HVL and TVL increase linearly. As shown in Table 8, the μ and μ_m decrease by 9.47% and 3.80% at 800 °C, respectively, compared to at room temperature, while the Mfp, thickness of HVL and TVL enhanced by 10.56%. By comparing

the results with the published literature, it is found that the trend of the μ of the LZTRSC is consistent with the RSC after the high-temperature treatment.

Figure 16 shows the relationship between the thickness and γ -ray transmission rate of the LZTRSC subjected to elevated temperatures. The results indicate that, at the same γ -ray transmission conditions, the minimum thickness of the γ -ray shielding layer of the concrete increases with the rise in temperature. From Figure 19, it can be found that, as the temperature rises, the deterioration of the LZTRST increases along with the increase in the width of the cracks, which may be due to the evaporation of the pore water. This results in a gradual decrease in the γ -ray shielding performance [39,71]. Thus, in the actual project, taking into account the special high-temperature environment, selecting the appropriate thickness of the LZTRSC can bring considerable economic and environmental benefits under the premise of satisfying the γ -ray shielding performance of the RSC.

After the high-temperature treatment, the mass of the LZTRSC is continually lost, accompanied with the decay in the ultrasonic wave velocity, which is not only reflected in the loss of strength, but also reflected in the γ -ray shielding properties of the attenuation for the RSC. The γ -ray shielding performance is mainly linked to the density of the RSC, and also linked to the concrete crack width [39]. When subjected to elevated temperatures, the internal cracks increase and expand. Some studies have shown that there is a great correlation between the crack width and the wave velocity [58]. Meanwhile, Lincheng et al. [37] found that the damage index (D) [72] fits well with the splitting strength, with R^2 values greater than 0.95. The rate of mass loss (M_s) and the D of the sacrificial RSC under the effect of elevated temperatures are introduced to evaluate the attenuation of γ -ray shielding subjected to different temperatures. The M_s and D are calculated by Equations (7) and (8), as follows:

$$M_s = \left(\frac{M - M_T}{M} \right) \times 100\% \quad (7)$$

$$D = \left[1 - \left(\frac{V_T}{V} \right)^2 \right] \times 100\% \quad (8)$$

where M_s represents the rate of mass loss of the LZTRSC after exposure to different high temperatures; M and M_T represent the mass of the LZTRSC at room temperature and after exposure to different high temperatures, respectively; D represents the index of damage of the LZTRSC after exposure to different high temperatures; V and V_T represent the wave velocity of the specimen of the LZTRSC at room temperature and after exposure to different high temperatures, respectively. Equation (8) is merely appropriate to the RSC which is naturally cooled after the heat treatment.

The rate of mass loss and the damage index after exposure to elevated temperatures are shown in Figures 21 and 22, from which the relationships between the rate of the mass loss, the damage index and the relative linear attenuation coefficient were obtained. The results are shown in Figures 23 and 24. On this basis, the appropriate function of the regression analysis was selected, whose results are shown in Figures 23 and 24. After exposure to different temperatures, the mass of the LZTRSC continuously decreases, which leads to a gradual increase in the damage index and a decrease in the density. Consequently, the γ -ray shielding property of the LZTRSC declines. This consequence indicates that the rate of the mass loss and damage index are all suitable methods for evaluating the degradation in the γ -ray shielding property after exposure to elevated temperatures. Furthermore, the correlation between the mass loss rate and the relative linear attenuation coefficient is stronger than that of the damage index. The γ -ray shielding property of the RSC is primarily influenced by the density of the concrete. However, magnetite exhibits better thermal stability, and after the heat treatment, the main factors affecting the concrete are water evaporation and the loss of water of crystallization. The high atomic number element content is not significantly reduced. Thus, the LZTRSC still retains a certain degree of its γ -ray shielding property after exposure to different high temperatures.

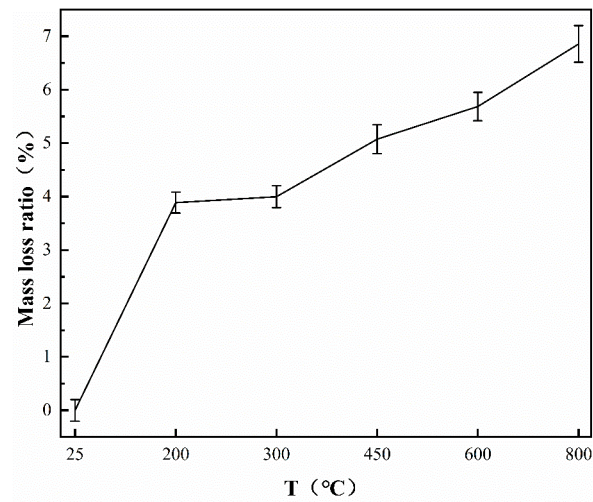


Figure 21. Rate of mass loss of the LZTRSC after exposure to high temperatures.

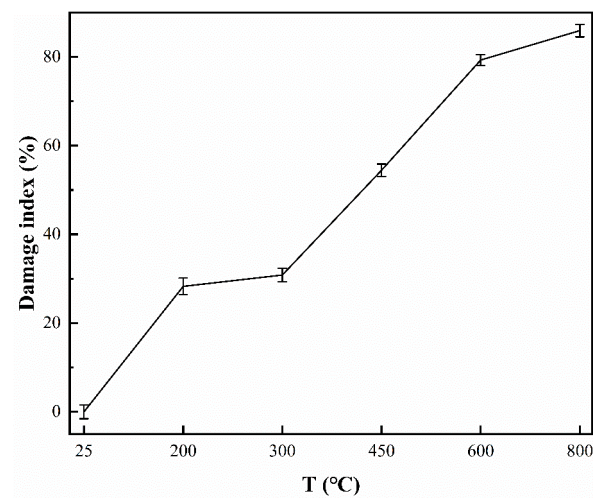


Figure 22. Damage index of the LZTRSC after exposure to high temperatures.

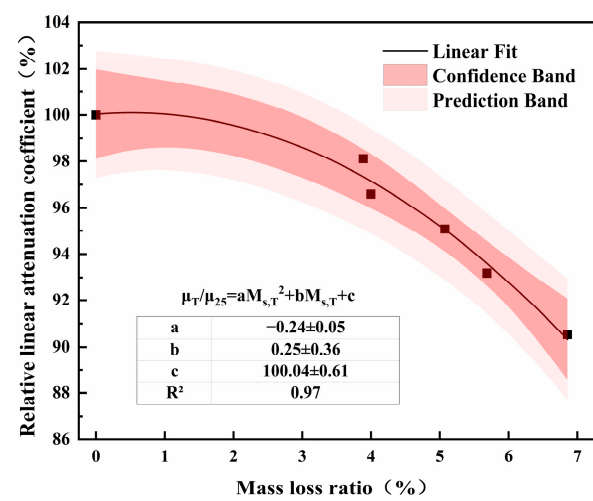


Figure 23. Relationship between mass loss ratio and relative linear attenuation coefficient after exposure to high temperatures.

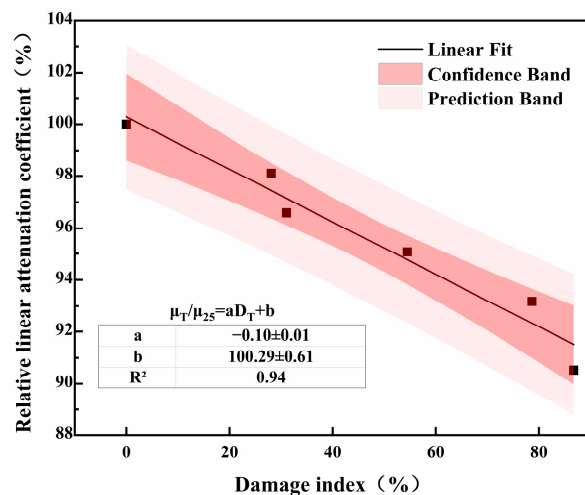


Figure 24. Relationship between the damage index and relative linear attenuation coefficient after exposure to high temperatures.

where μ_{25} and μ_T represent the linear attenuation coefficient at room temperature and at different temperatures, respectively.

The consequence of a leak in the RSC structure or vessel would be catastrophic. During the service period of the RSC, high-temperature treatment will be a major hidden danger. According to the above study, the γ -ray shielding performance of the RSC after high-temperature treatment has a high correlation with the damage index. Therefore, ultrasonic nondestructive testing technology will be used to detect the structure of the long-term exposure to high temperatures, as well as to predict and evaluate the residual γ -ray shielding performance after occasional exposure to high temperatures, similar to the role of fire, in the future.

4. Conclusions

- (1) According to the above study, lead–zinc tailings sand can be used as a suitable and sustainable substitute for fine aggregates in radiation shielding concrete, and can achieve good mechanical properties and γ -ray shielding performance at room temperature. In practical engineering applications, it is important to select an appropriate shielding layer thickness based on the temperature environment of the concrete. If a reasonable large-scale utilization of lead–zinc tailings sand can be achieved, it can bring considerable economic and environmental benefits.
- (2) By incorporating a dosage of 30% of the lead–zinc tailings sand, the workability and splitting tensile strength of the radiation shielding concrete can be improved. Moreover, this dosage can also achieve a high compressive strength and good gamma ray shielding performance, reaching up to 95.84% of the strength and 96.60% of the linear attenuation coefficient of the control group (0% dosage), respectively.
- (3) After exposure to elevated temperatures, the apparent degradation of the lead–zinc tailings radiation shielding concrete is mainly manifested by the generation, expansion and extension of cracks, with localized bursting occurring at 800 °C. The compressive strength shows an initial increase before 300 °C, followed by a linear decrease. Similarly, the splitting tensile strength exhibits a slight increase before 200 °C, but starts to decline beyond that temperature.
- (4) After exposure to elevated temperatures, the relative wave velocity shows a strong correlation ($R^2 > 0.95$) with both the compressive strength and splitting tensile strength, indicating that ultrasonic nondestructive testing is a suitable method for evaluating the extent of the damage to the mechanical properties of the lead–zinc tailings radiation shielding concrete.

- (5) After exposure to elevated temperatures, the mass loss rate, damage index and relative linear attenuation coefficient of the lead–zinc tailings radiation shielding concrete are closely related ($R^2 > 0.95$), which can be used to evaluate the remaining γ -ray shielding efficiency of the concrete. Between these factors, the mass loss rate exhibits a stronger correlation with the relative linear attenuation coefficient compared to the damage index.

Author Contributions: M.W.: Data curation, Formal analysis, and Writing—original draft. Z.C.: Funding acquisition, Methodology, Supervision, and Validation. Q.T.: Writing—review and editing. Y.Y.: Writing—review and editing, Supervision, and Validation. L.X.: Resources and Investigation. D.W.: Writing—review and editing. D.J.: Writing—review and editing. L.L.: Writing—review and editing. All authors have read and agreed to the published version of the manuscript.

Funding: This research was funded by National Natural Science Foundation of China [No. 51678286].

Data Availability Statement: The raw data supporting the conclusions of this article will be made available by the authors on request.

Conflicts of Interest: Author Liping Xie was employed by the company China Nuclear Industry 22ND Construction Co., Ltd. The remaining authors declare that the research was conducted in the absence of any commercial or financial relationships that could be construed as a potential conflict of interest.

References

- Ha, M.; Yoo, K.-Y.; Cho, S.-H. Glycophorin A mutant frequency in radiation workers at the nuclear power plants and a hospital. *Mutat. Res./Fundam. Mol. Mech. Mutagen.* **2002**, *501*, 45–56. [[CrossRef](#)] [[PubMed](#)]
- Başıyigit, C.; Akkurt, I.; Kilincarslan, S.; Beycioglu, A. Prediction of compressive strength of heavyweight concrete by ANN and FL models. *Neural Comput. Appl.* **2010**, *19*, 507–513. [[CrossRef](#)]
- Han, B.; Zhang, L.; Ou, J. (Eds.) Radiation Shielding Concrete. In *Smart and Multifunctional Concrete toward Sustainable Infrastructures*; Springer: Singapore, 2017; pp. 329–337.
- Chauhan, R.K.; Mudgal, M.; Verma, S.; Amritphale, S.S.; Das, S.; Shrivastva, A. Development and Design Mix of Radiation Shielding Concrete for Gamma-ray Shielding. *J. Inorg. Organomet. Polym. Mater.* **2017**, *27*, 871–882. [[CrossRef](#)]
- Abdullah, M.A.H.; Rashid, R.S.M.; Amran, M.; Hejazii, F.; Azreen, N.M.; Fediuk, R.; Voo, Y.L.; Vatin, N.I.; Idris, M.I. Recent Trends in Advanced Radiation Shielding Concrete for Construction of Facilities: Materials and Properties. *Polymers* **2022**, *14*, 2830. [[CrossRef](#)] [[PubMed](#)]
- Kanagaraj, B.; Anand, N.; Andrushia, A.D.; Naser, M.Z. Recent developments of radiation shielding concrete in nuclear and radioactive waste storage facilities—A state of the art review. *Constr. Build. Mater.* **2023**, *404*, 133260. [[CrossRef](#)]
- Binici, H.; Aksogan, O.; Sevinc, A.H.; Cinpolat, E. Mechanical and radioactivity shielding performances of mortars made with cement, sand and egg shells. *Constr. Build. Mater.* **2015**, *93*, 1145–1150. [[CrossRef](#)]
- Sevinç, A.H.; Durgun, M.Y. A novel epoxy-based composite with eggshell, PVC sawdust, wood sawdust and vermiculite: An investigation on radiation absorption and various engineering properties. *Constr. Build. Mater.* **2021**, *300*, 123985. [[CrossRef](#)]
- Mahmoud, K.A.; Sayyed, M.I.; Almuqrin, A.H.; Elhelaly, M.A.; Alhindawy, I.G. Synthesis of glass powders for radiation shielding applications based on zirconium minerals' leach liquor. *Radiat. Phys. Chem.* **2023**, *207*, 110867. [[CrossRef](#)]
- Alwaeli, M.; Nadziakiewicz, J. Recycling of scale and steel chips waste as a partial replacement of sand in concrete. *Constr. Build. Mater.* **2011**, *28*, 157–163. [[CrossRef](#)]
- Alwaeli, M. The implementation of scale and steel chips waste as a replacement for raw sand in concrete manufacturing. *J. Clean. Prod.* **2016**, *137*, 1038–1044. [[CrossRef](#)]
- Beaucour, A.-L.; Pliya, P.; Faleschini, F.; Njinwoua, R.; Pellegrino, C.; Noumowé, A. Influence of elevated temperature on properties of radiation shielding concrete with electric arc furnace slag as coarse aggregate. *Constr. Build. Mater.* **2020**, *256*, 119385. [[CrossRef](#)]
- Alwaeli, M. Investigation of gamma radiation shielding and compressive strength properties of concrete containing scale and granulated lead-zinc slag wastes. *J. Clean. Prod.* **2017**, *166*, 157–162. [[CrossRef](#)]
- Binici, H.; Aksogan, O.; Sevinc, A.H.; Kucukonder, A. Mechanical and radioactivity shielding performances of mortars made with colemanite, barite, ground basaltic pumice and ground blast furnace slag. *Constr. Build. Mater.* **2014**, *50*, 177–183. [[CrossRef](#)]
- Attia, M.M.; Abdelsalam, A.B.; Mohamed, A.; Saad, A.I.; Farouk, A.M. Metal-Nails Waste and Steel Slag Aggregate as Alternative and Eco-Friendly Radiation Shielding Composites. *Buildings* **2022**, *12*, 1120. [[CrossRef](#)]
- Cano, N. Evaluation of the extractive gold process: Open-pit mining through exergy analysis. *J. Sustain. Min.* **2020**, *19*, 3. [[CrossRef](#)]

17. Lyu, Z.; Chai, J.; Xu, Z.; Qin, Y.; Cao, J. A Comprehensive Review on Reasons for Tailings Dam Failures Based on Case History. *Adv. Civ. Eng.* **2019**, *2019*, 4159306. [[CrossRef](#)]
18. Hamilton, A.K.; Laval, B.E.; Petticrew, E.L.; Albers, S.J.; Allchin, M.I.; Baldwin, S.A.; Carmack, E.C.; Déry, S.J.; French, T.D.; Granger, B.; et al. Seasonal Turbidity Linked to Physical Dynamics in a Deep Lake Following the Catastrophic 2014 Mount Polley Mine Tailings Spill. *Water Resour. Res.* **2020**, *56*, e2019WR025790. [[CrossRef](#)]
19. Davies, M. Tailings Impoundment Failures: Are Geotechnical Engineers Listening? *Waste Geotech.* **2002**, *20*, 31–36.
20. Vrhovnik, P.; Dolenc, T.; Serafimovski, T.; Dolenc, M.; Rogan Šmuc, N. The occurrence of heavy metals and metalloids in surficial lake sediments before and after a tailings dam failure. *Pol. J. Environ. Stud.* **2013**, *22*, 1525–1538.
21. Felizardo, J.P.; Muniz, M.C.; Vezzoni, M.; Cardoso, R.P.; Wasserman, J.; Padilla, R.; Migliori, A.; Anjos, R.M. Sources of sedimentary organic matter and assessment of heavy-metal levels in estuarine sediments after Fundão dam breach. *Estuar. Coast. Shelf Sci.* **2021**, *261*, 107507. [[CrossRef](#)]
22. Lv, X.D.; Liu, Z.A.; Zhu, Z.G.; Li, B.X. Study of the progress of tailings comprehensive utilization of raw materials in cement and concrete. *Mater. Rep.* **2018**, *32*, 452–456. (In Chinese)
23. Hu, G.; Zhang, C.; Qian, C.; Wen, J. Recent research progress of compressive utilization of molybdenum tailings resources. *Mater. Rep.* **2019**, *33* (Suppl. S2), 233–238. (In Chinese)
24. Lu, C.; Chen, H.Y.; Fu, L.J.; Tian, G.; Zhang, H.; Liang, J.; Yang, H. Research progress on the preparation of new building materials using iron tailings. *Mater. Rep.* **2021**, *35*, 5011–5026. (In Chinese)
25. Zhang, Y.; Li, Z.; Gu, X.; Nehdi, M.L.; Marani, A.; Zhang, L. Utilization of iron ore tailings with high volume in green concrete. *J. Build. Eng.* **2023**, *72*, 106585. [[CrossRef](#)]
26. Yanjie, T.; Liang, Z.; Bo, L.; Wei, C. Controlling the soundness of Portland cement clinker synthesized with solid wastes based on phase transition of MgNiO₂. *Cem. Concr. Res.* **2022**, *157*, 106832.
27. Saedi, A.; Jamshidi-Zanjani, A.; Darban, A.K. A review on different methods of activating tailings to improve their cementitious property as cemented paste and reusability. *J. Environ. Manag.* **2020**, *270*, 110881. [[CrossRef](#)] [[PubMed](#)]
28. Yao, G.; Liu, Q.; Wang, J.; Wu, P.; Lyu, X. Effect of mechanical grinding on pozzolanic activity and hydration properties of siliceous gold ore tailings. *J. Clean. Prod.* **2019**, *217*, 12–21. [[CrossRef](#)]
29. Saedi, A.; Jamshidi-Zanjani, A.; Mohseni, M.; Khodadadi Darban, A.; Nejati, H. Mechanical activation of lead–zinc mine tailings as a substitution for cement in concrete construction. *Constr. Build. Mater.* **2023**, *364*, 129973. [[CrossRef](#)]
30. Çullu, M.; Ertaş, H. Determination of the effect of lead mine waste aggregate on some concrete properties and radiation shielding. *Constr. Build. Mater.* **2016**, *125*, 625–631. [[CrossRef](#)]
31. Gallala, W.; Hayouni, Y.; Gaied, M.E.; Fusco, M.; Alsaied, J.; Bailey, K.; Bourham, M. Mechanical and radiation shielding properties of mortars with additive fine aggregate mine waste. *Ann. Nucl. Energy* **2017**, *101*, 600–606. [[CrossRef](#)]
32. Çullu, M.; Bakırhan, E. Investigation of radiation absorption coefficients of lead-zinc mine waste rock mixed heavy concrete at 662–1460 keV energy range. *Constr. Build. Mater.* **2018**, *173*, 17–27. [[CrossRef](#)]
33. Chen, Z.; Xiao, L.; Tao, Q.; Xie, L. Research on the effect of lead-zinc tailings sand on the shielding performance of concrete to gamma ray. *Ind. Constr.* **2019**, *49*, 133–137. (In Chinese) [[CrossRef](#)]
34. Chen, Z.; Cai, S.; Tao, Q.; Zhang, Z. Compressive strength and shielding performance of lead-zinc tailing concrete. *Concrete* **2021**, *2*, 68–71+76. (In Chinese)
35. Cherdron, W. The interaction of burning sodium with concrete. In Proceedings of the European Nuclear Conf. (ENC '90), Lyon, France, 23–28 September 1990.
36. Sakr, K.; El-Hakim, E. Effect of high temperature or fire on heavy weight concrete properties. *Cem. Concr. Res.* **2005**, *35*, 590–596. [[CrossRef](#)]
37. Lincheng, L.; Zhenfu, C.; Qiuwang, T.; Liping, X.; Dan, J.; Zhujing, L.; Du, D. Effects of high temperatures on the splitting tensile strength and gamma ray shielding performance of radiation shielding concrete. *Constr. Build. Mater.* **2022**, *343*, 127953.
38. Lv, Y.; Qin, Y.; Wang, J.; Li, G.; Zhang, P.; Liao, D.; Xi, Z.; Yang, L. Effect of incorporating hematite on the properties of ultra-high performance concrete including nuclear radiation resistance. *Constr. Build. Mater.* **2022**, *327*, 126950. [[CrossRef](#)]
39. Lee, C.-M.; Lee, Y.H.; Lee, K.J. Cracking effect on gamma-ray shielding performance in concrete structure. *Prog. Nucl. Energy* **2007**, *49*, 303–312. [[CrossRef](#)]
40. Gencil, O. Effect of elevated temperatures on mechanical properties of high-strength concrete containing varying proportions of hematite. *Fire Mater.* **2012**, *36*, 217–230. [[CrossRef](#)]
41. Rashid, R.S.M.; Salem, S.M.; Azreen, N.M.; Voo, Y.L.; Haniza, M.; Shukri, A.A.; Yahya, M.-S. Effect of elevated temperature to radiation shielding of ultra-high performance concrete with silica sand or magnetite. *Constr. Build. Mater.* **2020**, *262*, 120567. [[CrossRef](#)]
42. Oto, B.; Yıldız, N.; Korkut, T.; Kavaz, E. Neutron shielding qualities and gamma ray buildup factors of concretes containing limonite ore. *Nucl. Eng. Des.* **2015**, *293*, 166–175. [[CrossRef](#)]
43. El-Samrah, M.G.; Abdel-Rahman, M.A.E.; El Shazly, R.M. Effect of heating on physical, mechanical, and nuclear radiation shielding properties of modified concrete mixes. *Radiat. Phys. Chem.* **2018**, *153*, 104–110. [[CrossRef](#)]
44. Masoud, M.A.; Kansouh, W.A.; Shahien, M.G.; Sakr, K.; Rashad, A.M.; Zayed, A.M. An experimental investigation on the effects of barite/hematite on the radiation shielding properties of serpentine concretes. *Prog. Nucl. Energy* **2020**, *120*, 103220. [[CrossRef](#)]
45. GB 175-2007; Common Portland Cement. Standardization Administration: Beijing, China, 2007.

46. GB/T 14684-2022; Sand for Construction. Standardization Administration: Beijing, China, 2022.
47. GB/T 14685-2022; Pebble and Crushed Stone for Construction. Standardization Administration: Beijing, China, 2022.
48. GB/T 34008-2017; Radiation Shielding Concrete. Standardization Administration: Beijing, China, 2017.
49. GB/T 50081-2019; Standard for Test Method of Concrete Physical and Mechanical Properties. Ministry of Housing and Urban-Rural Development of the People's Republic of China: Beijing, China, 2019.
50. CECS21:2000; Technical Specification for Inspection of Concrete Defects by Ultrasonic Method. China Association for Engineering Construction Standardization: Beijing, China, 2000.
51. Ouda, A.S. Development of high-performance heavy density concrete using different aggregates for gamma-ray shielding. *Prog. Nucl. Energy* **2015**, *79*, 48–55. [[CrossRef](#)]
52. Wang, J.; Liu, C. *Introduction to Nuclear Technology and Radiation Protection*; China University of Petroleum Press: Beijing, China, 2012; ISBN 9787563638093. (In Chinese)
53. Zhao, Z.; Chen, W.; Li, Q.; Yuan, S.; Peng, R. Effect of Fine Tailings on Strength Properties and Microstructure of Tailings Backfill. *J. Wuhan Univ. Technol.* **2018**, *40*, 16–21. (In Chinese)
54. Alieh, S.; Ahmad, J.-Z.; Khodadadi, D.A.; Mehdi, M.; Hamidreza, N. Utilization of lead–zinc mine tailings as cement substitutes in concrete construction: Effect of sulfide content. *J. Build. Eng.* **2022**, *57*, 104865.
55. Li, M.; Qian, C.; Wang, H.; You, Y.; Sun, W. Mechanical properties of high-strength concrete after fire. *J. Chin. Ceram. Soc.* **2003**, *31*, 1116–1120. (In Chinese) [[CrossRef](#)]
56. Wang, L.; Zhang, Q.; Yi, J.; Zhang, J. Effects of coral aggregate properties on the ultrasonic pulse velocity of concrete. *J. Build. Eng.* **2023**, *80*, 107935. [[CrossRef](#)]
57. Dias, A.R.d.O.; Amancio, F.A.; Rafael, M.F.d.C.; Cabral, A.E.B. Study of propagation of ultrasonic pulses in concrete exposed at high temperatures. *Procedia Struct. Integr.* **2018**, *11*, 84–90. [[CrossRef](#)]
58. Hwang, E.; Kim, G.; Choe, G.; Yoon, M.; Gucunski, N.; Nam, J. Evaluation of concrete degradation depending on heating conditions by ultrasonic pulse velocity. *Constr. Build. Mater.* **2018**, *171*, 511–520. [[CrossRef](#)]
59. Candelaria, M.D.E.; Kee, S.-H. Evaluation of thermal damages of concrete subjected to high temperatures using recurrent neural networks for ultrasonic pulse waves. *Constr. Build. Mater.* **2023**, *407*, 133416. [[CrossRef](#)]
60. Wu, C. The Study on Strong Radiation Shielding Concrete Test of Nuclear Engineering. Ph.D. Thesis, Central South University, Changsha, China, 2008. (In Chinese).
61. Fillmore, D.L. *Literature Review of the Effects of Radiation and Temperature on the Aging of Concrete*; Idaho National Lab. (INL): Idaho Falls, ID, USA, 2004.
62. Memon, S.A.; Shah, S.F.A.; Khushnood, R.A.; Baloch, W.L. Durability of sustainable concrete subjected to elevated temperature—A review. *Constr. Build. Mater.* **2019**, *199*, 435–455. [[CrossRef](#)]
63. Lu, T.; Zhao, G.; Lin, Z.S.; Yue, Q. Microscopic Analysis of Long Standing Concrete after High Temperature. *J. Build. Mater.* **2003**, *6*, 135–141. (In Chinese)
64. Arioz, O. Effects of elevated temperatures on properties of concrete. *Fire Saf. J.* **2007**, *42*, 516–522. [[CrossRef](#)]
65. Liu, X.; Yuan, Y.; Ye, G.; Schutter, G.D. Study on Pore Structure Evolution of High Performance Concrete with Elevated Temperatures. *J. Tongji Univ. Nat. Sci.* **2008**, *36*, 1473–1478. (In Chinese)
66. Sanaz, R.; Hamzeh, H. The Effects of Supplementary Cementitious Materials (SCMs) on the Residual Mechanical Properties of Concrete after Exposure to High Temperatures—Review. *Buildings* **2022**, *13*, 103. [[CrossRef](#)]
67. Zhu, Q.; Yuan, Y.; Chen, J.-h.; Fan, L.; Yang, H. Research on the high-temperature resistance of recycled aggregate concrete with iron tailing sand. *Constr. Build. Mater.* **2022**, *327*, 126889. [[CrossRef](#)]
68. Kim, G.-Y.; Kim, Y.-S.; Lee, T.-G. Mechanical properties of high-strength concrete subjected to high temperature by stressed test. *Trans. Nonferrous Met. Soc. China* **2009**, *19* (Suppl. S1), 128–133. [[CrossRef](#)]
69. Min, H.C.; Ing, D.S.; Choo, C.S.; Xiaofeng, L. The effect of particle sizes of steel slag as cement replacement in high strength concrete under elevated temperatures. *Constr. Build. Mater.* **2024**, *411*, 134531.
70. Venkata, S.K.N.; Satyanarayana, S.V. Effect of elevated temperatures on the flexural strength of crushed rock dust concrete. *Mater. Today Proc.* **2021**, *42 Pt 2*, 1176–1183.
71. Kara, U.; Issa, S.A.M.; Yorgun, N.Y.; Kilicoglu, O.; Rashad, M.; Abuzaid, M.M.; Kavaz, E.; Tekin, H.O. Optical, structural and gamma ray shielding properties of dolomite doped lithium borate glasses for radiation shielding applications. *J. Non-Cryst. Solids* **2020**, *539*, 120049. [[CrossRef](#)]
72. Zhu, H.Y.; Sun, W.; Jiang, J.Y. Damage Evolution of Sacrificial Concrete Subjected to Elevated Temperatures. *J. Chin. Ceram. Soc.* **2016**, *44*, 211–217. (In Chinese) [[CrossRef](#)]

Disclaimer/Publisher's Note: The statements, opinions and data contained in all publications are solely those of the individual author(s) and contributor(s) and not of MDPI and/or the editor(s). MDPI and/or the editor(s) disclaim responsibility for any injury to people or property resulting from any ideas, methods, instructions or products referred to in the content.